Featured in Physics

Active Mie-like resonance for noninvasive glucose detection

Hoyeong Kwon[1,*] and Andrea Alù[2,3,†]

[1] *Center for Advanced Meta-Materials, Daejeon, 34103, Republic of Korea*

[2] *Photonics Initiative, Advanced Science Research Center, City University of New York, New York, New York 10031, USA*

[3] *Physics Program, Graduate Center, City University of New York, New York, New York 10016, USA*

(Received 26 November 2023; revised 13 February 2024; accepted 15 February 2024; published 28 March 2024)

An ideal toolset to diagnose diabetes consists of an in-hand portable device that can effectively detect glucose concentration in the blood in real time without having to perforate the skin. However, existing glucose monitoring systems are invasive, and those that are noninvasive have low accuracy. Here, we explore an alternative approach for noninvasive monitoring of the glucose concentration in blood. We excite Mie-like resonances within highly lossy media by introducing active loads, uniformly applied within the inner circumference of a dielectric ring structure. Our study opens a possible way of developing portable glucose monitoring systems that can detect the glucose concentration with a noninvasive approach and improved accuracy compared with existing techniques.

DOI: 10.1103/PhysRevApplied.21.034060

As life expectancy and adult disease incidence rates increase simultaneously, diagnosing diseases has become of major relevance in modern medicine [1–4]. Since most adult diseases are chronic, the ability to track them at an early stage is vital, which requires the development of simple and convenient medical diagnostic devices [5–7]. Portable devices offer patients the opportunity to track their conditions in real time. In this context, recent studies have focused on the development of glucose level monitors for the purpose of diagnosing diabetes at an early stage [8]. For diabetes, it is important to monitor the glucose level in the blood constantly rather than getting a medical checkup after showing pathological symptoms [9–11]. So far, most of the existing techniques for glucose monitoring are invasive, where patients are periodically required to draw their blood, or semipermanently insert tubes into blood vessels or in the dermis for constant glucose monitoring [12–14].

Since typical methods induce constant pain and put a strain on the patient, electromagnetic methods for noninvasively measuring the glucose level are actively being pursued over various frequency ranges [15–28]. For instance, approaches to measure the current conductivity of tears or interstitial fluid under the skin have been proposed in several studies [18,19]. This approach utilizes a body-attachable device, such as smart lenses or tattoo antennas on the skin. An alternative approach close to commercialization relies on Raman spectroscopy [20–23]. This approach interrogates the electromagnetic properties of glucose molecules by exciting the skin with a laser at specific frequencies. The detection is performed through scattering spectroscopy, which is affected by the glucose concentration. Similarly, measuring the absorption efficiency in the near-infrared spectrum has been proposed, since absorption is affected by the glucose concentration inside the interstitial fluid [24–28].

However, these methods come with limitations, such as degraded monitoring accuracy and limits on developing practical devices. First, measuring the current conductivity of interstitial fluid or tears is often unreliable for diagnosing diabetes, since there are many variables that may affect the current conductivity beyond the glucose concentration, e.g., unwanted interstitial electrolytes [29]. In the case of Raman spectroscopy, it is easy to apply as a watch or body-attached sensor. However, considering that the laser does not effectively penetrate the skin thickness or capillary vessels, it is hard to be sure whether the response comes from changes in the glucose level inside the capillary or in other tissues such as the dermis [30]. Considering that diabetic symptoms are directly affected by the glucose inside the capillary vessels, this is a critical issue to be solved. Finally, absorption measurements in the near-infrared spectrum are also known to be less accurate as they are influenced by the level of melanin distribution and tissue composition of the skin [31].

In the rf spectrum, glucose monitoring is limited by the large absorption loss of the body tissue and fluid, which drastically reduces the monitoring accuracy [32–35]. To overcome these limitations, studies on monitoring

---

[*] hoyeong3958@kimm.re.kr
[†] aalu@gc.cuny.edu

glucose levels on the earlobe or finger wedge have been performed in the *V* band (40–75 GHz) by applying waveguide structures that sandwich skin-capillary-skin layers. This approach takes advantage of thin layered structures, minimizing the inherent loss. However, the loss from the tissue remains large, often preventing accurate detection. Additionally, the proposed waveguide equipment is bulky and difficult to carry, thus impractical [34]. Recently, we have been exploring active shunt loads applied to the skin-capillary-skin geometry (earlobe or finger wedge) to enhance the monitoring accuracy. By applying an active load to one side of the skin, the entire structure can experience an anisotropic transmission resonance (ATR) at a certain frequency, enhancing sensitivity [36]. Based on this principle, we explored a way to realize this active load by employing a negative impedance converter (NIC) circuit, and prove that the ATR response is linearly tuned by the glucose concentration, offering a convenient way to enhance diabetes testing devices. This approach offers enhanced sensitivity, enabling a glucose level detection of 0.01 wt % per 100 kHz between 4 and 6 GHz [37]. The active loading compensates for the absorption loss in the biological media, while the overall signal-to-noise ratio remains limited.

In this paper, we explore an enhanced scheme for glucose monitoring, designed to be practically implemented as a portable gadget while enhancing glucose monitoring sensitivity. To satisfy these requirements, a ring-shaped glucose sensor applied to a single finger is proposed. The ring is composed of SiO_2 with Cu plates sandwiching the SiO_2 ring structure. In the open cylindrical structure, the ATR response is difficult to achieve, since the response is applicable to two-port systems [36]. Instead, we excite a Mie-like resonance within concentric cylindrical media of skin-capillary-bone to effectively monitor the glucose concentration within the finger. To excite such a resonance in lossy media, active loads are uniformly applied around the inner circumference of the ring. Supported by these active loads, the Mie-like resonance is strongly enhanced. At the resonance frequency, the field shows a Mie-like resonance pattern, with a typical ϕ dependence ($\cos m\phi$, m is an integer) in its angular pattern. The field at resonance is strongly localized inside the skin and the capillary tissue, effectively providing a mechanism to monitor the glucose concentration inside the capillary layer.

In the following, we first introduce the geometry of the ring structure, then we numerically simulate the optimized structure and outline the underlying resonance mechanism. The resonance responses with different values of active loads and thicknesses of the tissue layers are studied to confirm the stability of the proposed method. Finally, glucose monitoring inside the capillary layer is explored, demonstrating that the Mie-like resonance linearly shifts along the frequency axis with increasing glucose concentration. Our calculations indicate over 3 times enhanced sensitivity compared with prior studies using active loading, supporting an different type of glucose monitor with a single ring, which may effectively monitor the glucose level with enhanced sensitivity at a finger.

We consider a ring wrapper around a single finger, as shown in Fig. 1(a). The structure is simplified to a concentric cylindrical pillar composed of skin, capillary, and bone with radii r_s, r_g, and r_b, respectively. The radial thickness of each layer is defined as $t_s = r_s - r_g$, $t_g = r_g - r_b$, and $t_b = r_b$. Each parameter is defined assuming that the ring is wrapped around the index finger of a human body, and the height of the finger is $h_f = 7 - 10$ cm [38]. Figure 1(b) shows the ring structure integrated with active loads. Here, the inner radius of the ring is r_s, and the outer radius is defined as r_o. The thickness and height of the ring are t_r and h_r, respectively. The top and bottom of the ring are grounded with Cu plates to localize the field. Active loads are designed to be conformal rectangular shapes with height h_y, and arc length c_y, applied symmetrically following the inner circumference of the ring with 60° steps. Here, the arc length c_y has a 30° arc length and the active load has a negative admittance value $Y_{s,z}[\text{Siemens}] = -1/Z_{s,z}$ ($Z_{s,z}$ is a positive integer). The

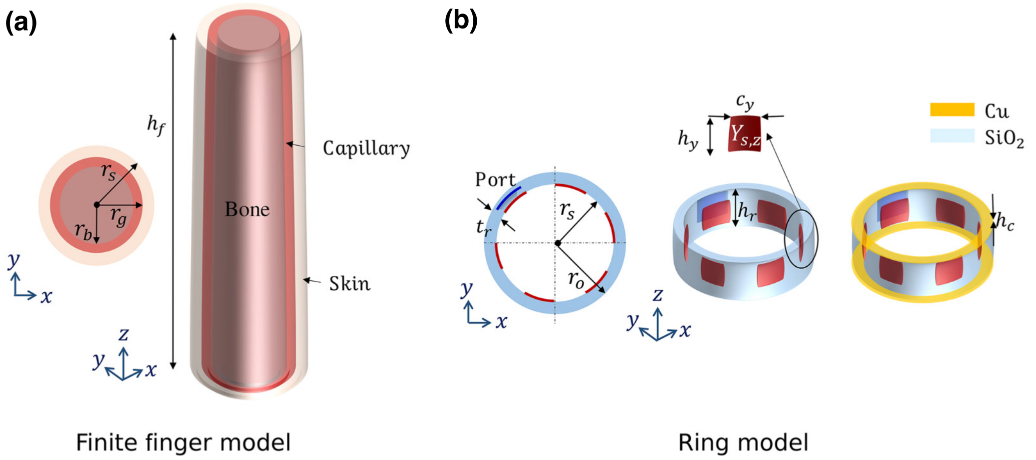

Finite finger model

Ring model

FIG. 1. (a) A finite model of the finger, simplified to a concentric cylindrical structure composed of bone, capillary, and skin. The radius of each cylinder is defined as r_s, r_g, r_b from the center and the finger height is h_f. (b) Illustration of the ring integrated with active loads. The upper and lower portions of the ring are grounded with Cu plates.

major reason for the symmetric placement of the active loads is to uniformly excite the resonance to cover the lossy medium in its entirety. The transmit port (blue arc) is applied inside the ring with a 30° arc length and generates and electric field E_z pointing in the direction of the finger's center, $\hat{\rho}$. A spacer of height h_c is introduced between the Cu plates and the active loads on the top and bottom to prevent electrical shorting between them.

We perform numerical calculations using COMSOL Multiphysics 6.0, as shown in Fig. 2(a). The upper-left figure shows the top view of the structure with the ring worn on the finger. An air layer is applied with scattering boundary conditions at the outmost surface, and a perfectly matched layer (PML) is applied before the scattering boundary condition. The right panel shows the longitudinal view of the finger. In the simulations, the height of the ring h_r is changed to tune the resonance, and h_y and h_p are defined as $0.8h_r$ and $0.9h_r$, respectively, and the spacer height h_c and the thickness of Cu plates are both set at $0.05h_r$. Other parameters, such as radii and arc lengths of the active load, are kept constant. The electromagnetic properties of the media are calculated analytically at the frequency of interest. First, the relative permittivity of the skin and the bone are derived using the Cole-Cole dispersion model, as discussed in Ref. [39]. For the capillary layer, the permittivity of blood is replaced by the permittivity of a glucose-water solution, considering that the blood condition differs by person and changes with time. The blood is composed of various components and the blood permittivity can vary depending on the patient's condition. However, the blood permittivity measured in different patients has the same tendency of decreasing with large glucose concentration, with a variation $\Delta\varepsilon \sim 5$ [40]. Therefore, we assume that the impact from blood components is negligible and the permittivity is stable with time. The differences associated with individual patients and the permittivity changes in time will be addressed in a calibration process during practical device development. In this study, the glucose-water permittivity is derived using the Debye model, as provided in Ref. [41], where the calculated permittivity is in the same range as the permittivity measured in Ref. [40]. In the calculation, the glucose concentration of the solution is varied from 0 to 4 wt %, where the weight percentage (wt %) is the percentage of solute mass divided by solution mass in this study. The relative permittivities of skin, bone, and the glucose-water solution are provided in Fig. 2(b). Here, we can see that the relative permittivity of skin and bone are relatively stable

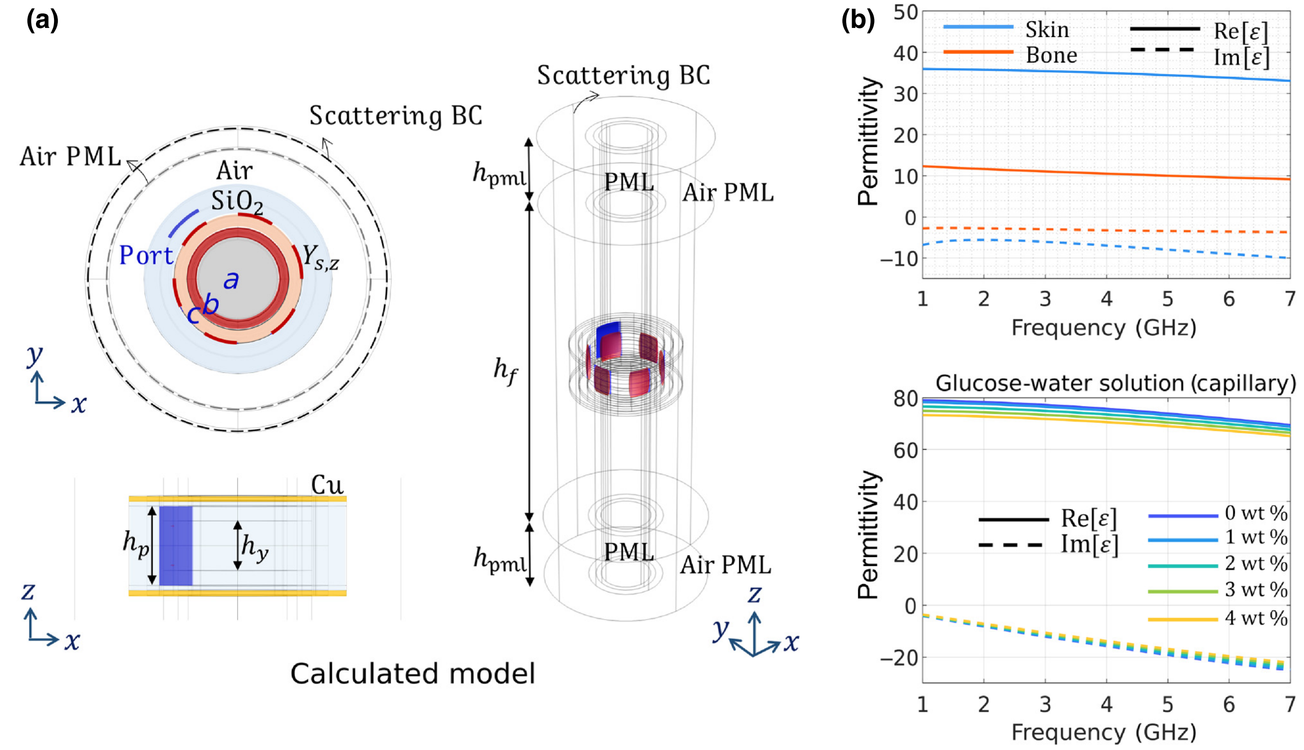

FIG. 2. (a) Simulated model of Figs. 1(a) and 1(b) in COMSOL Multiphysics 6.0. The ring is worn on the finger. The transmit port (blue arc) is applied inside the ring (blue area). The copper plates are positioned to sandwich the ring to support the resonance. Here, area "*a*" is the bone, "*b*" is the capillary and "*c*" is the skin. The entire finger model is defined with length h_f with two h_{pml} layers; scattering boundary condition (BC) and PML condition are applied properly to model wave propagation. (b) (Upper panel) Relative permittivity of skin and bone. (Lower panel) Relative permittivity of glucose-water solutions from 0 to 4 wt %.

at the frequency of interest, where the variations of both real and imaginary parts are $\Delta\varepsilon \leq 5$. Compared to the relative permittivity of skin and bone, the relative permittivity of glucose-water solutions varies 4 to 5 times more both in real and imaginary parts. This property ensures that the resonance is mostly affected by the glucose-water solution rather than skin or bone.

We first simulate the structure without active loads to confirm that the proposed ring model in Fig. 2(a) can support a Mie-like resonance. The port is excited with $E_z = 1\,\mathrm{V/m}$ with power $\vec{P}_{\rm port} = \hat{\rho} A_{\rm port}(|E_z|^2/\eta_{\rm SiO_2})$, and the excited power is changed by the height of the port h_p (where $A_{\rm port} = h_p c_p$). The c_p is the arclength of port that is stable in the calculation. To monitor the resonance from the structure, the $\hat{\rho}$ component of the radiated intensity $\vec{p}_{\rm rad}$ at the outer surface of the ring is integrated as

$$P_{\rm rad} = \int_0^{h_p} \int_0^{2\pi} \hat{\rho} \cdot \vec{p}_{\rm rad}\, r_o d\varphi dz.$$

For this calculation, the glucose concentration is set at 0 wt %, and the results are shown in Fig. 3(a). To figure out the resonance properties, the calculation is performed by changing the height of the ring h_r from 5 to 15 mm with fixed r_o, and the calculated $P_{\rm rad}$ is provided as a contour plot. In the plot, we can observe evident Mie-like resonances, for which the azimuthal order increases with frequency from TM_{11} to TM_{41}. The field is highly localized inside the finger for larger azimuthal orders. In contrast, the Fabry-Perot mode or radial modes are not observed for this geometry, and only azimuthal resonances are excited. In the case of a cylinder uniformly composed of a single dielectric material, it is natural to excite both m and n modes ($m =$ azimuthal mode, $n =$ radial mode). However, the structure in this study is partially grounded with copper plates in the radial direction, which alters the radial mode resonance. Therefore, only azimuthal modes are excited in the proposed ring structure, benefitting glucose monitoring since the fields are uniform in the radial and axial directions.

Next, the material loss in the finger and active loads $Y_{s,z} = -1/Z_{s,z}$ are added in the calculation and the simulated results are provided in Fig. 3(b). $Z_{s,z}$ is set to be 38 Ω and the other parameters remain the same. The results show that $P_{\rm rad}$ decreases due to the large loss in the entire frequency regime. However, supported by active loads that are uniformly applied to the finger, a Mie-like resonance is excited analogous to Fig. 3(a). Even though higher-order modes are not clearly excited due to the increased loss at higher frequencies, the active loads support the field enhancement and preserve the Mie-like resonance. To enhance the resonant response for higher azimuthal modes, the admittance value of the active loads is changed with $Z_{s,z} = 40\ \Omega$, and the result compared to the result for $Z_{s,z} = 38\ \Omega$ is provided in Fig. 4(a). $P_{\rm rad}$ at resonance shows no large difference between the different active loads, since the gain is only slightly increased. The resonance frequency is also stable, without a big shift. However, at $h_r = 10$ mm, TM_{31} is strongly excited at 5.1 GHz, where no resonance was excited in the previous

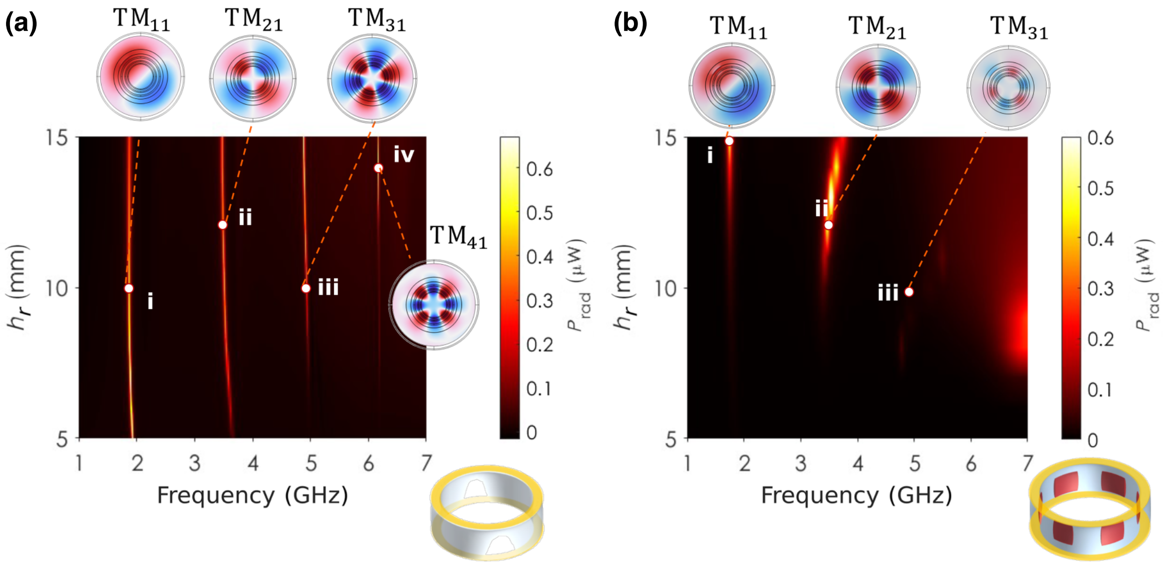

FIG. 3. (a) Mie-like resonance with lossless finger wearing the ring without active loads. The azimuthal modes are excited with respect to the frequency axis. E_z field plotted when the height of the ring h_r is (i) 10 mm, (ii) 12 mm, (iii) 10 mm, (iv) 14 mm, calculated at the mid-height of the ring. (b) Mie-like resonance with material loss in the finger. Now, the ring is integrated with active loads around the inner circumference of the ring. The E_z field is plotted when the height of the ring $h_r$is (i) 15 mm, (ii) 12 mm, (iii)10 mm.

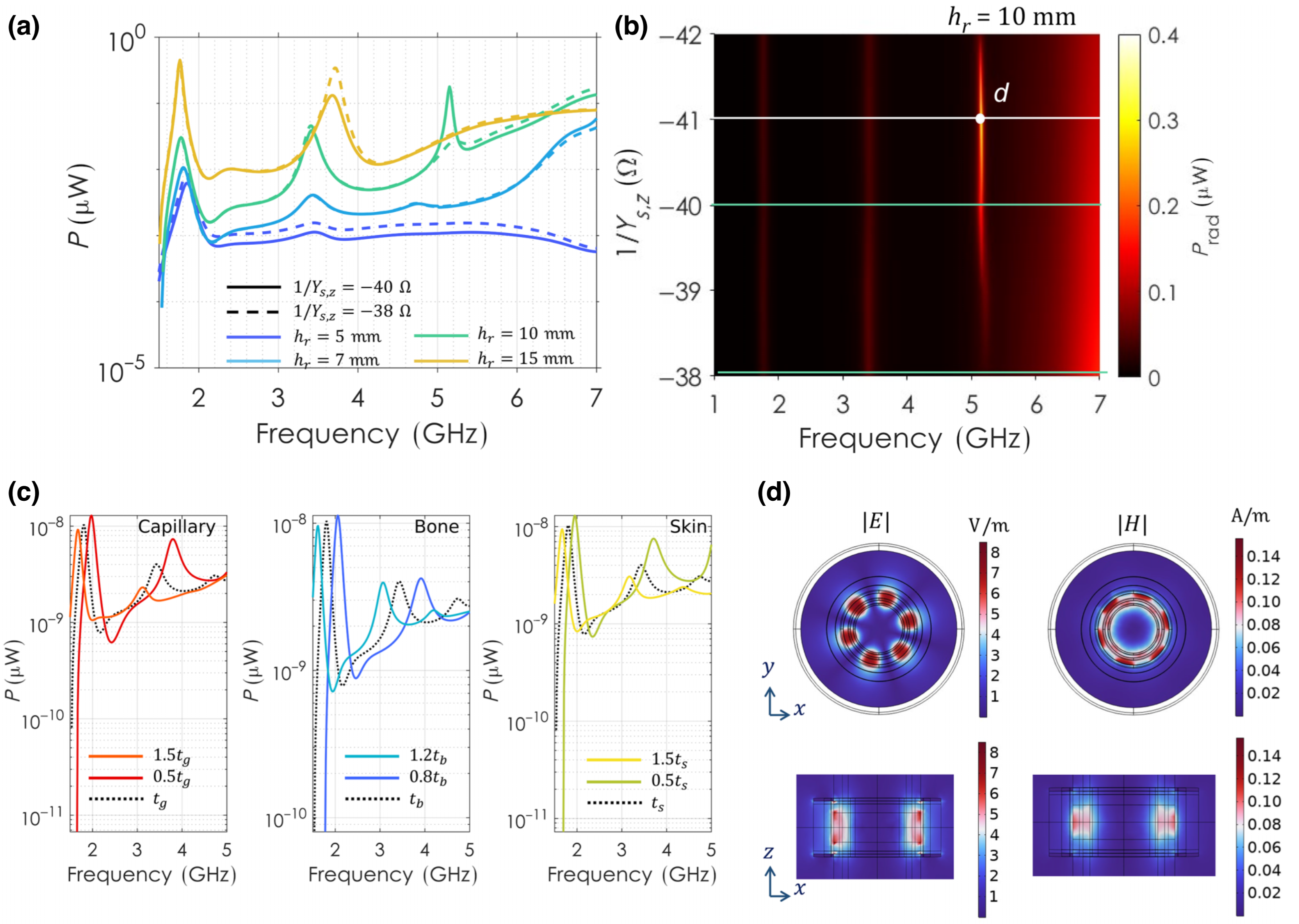

FIG. 4. (a) Radiated power P_{rad} comparison between the case with $1/Y_{s,z} = -40\ \Omega$ (solid line) and that with $1/Y_{s,z} = -38\ \Omega$ (dashed line). The admittance value of active loads differs from the calculated results in (b). The height of the ring is $h_r = 5$, 10, 7, 15 mm. (b) Radiated power P_{rad} with different active loads, with $1/Y_{s,z}$ from −38 to −42 Ω. Here, the height of the ring h_r is 10 mm. The green line is the same as in (a) when h_r is 10 mm. (c) Radiated power P_{rad} when the thicknesses of capillary, bone, and skin layers are changed. (d) Magnitude of electric and magnetic fields at point d in (b). The field is calculated at the mid-height of the ring.

calculation. To confirm that the gain admittance value affects the Mie-like resonance response, the simulation is performed after changing $Z_{s,z} = 38\ \Omega$ to $Z_{s,z} = 42\ \Omega$ with fixed ring height $h_r = 10$ mm and the result is provided in Fig. 4(b). The results show the frequency of each Mie-like resonance is stable with respect to the active load value. However, the magnitude at the resonance frequency is changed, giving the strongest response at $Z_{s,z} = 41\ \Omega$, which appears to conjugate match the loss for this mode.

To prove that the resonance response is stable with respect to different dimensions of the finger, we calculate the response for different radial thicknesses of each layer (skin, capillary, and bone) in Fig. 4(c). The calculation is performed with 0 wt % glucose-water solution, and the active load and height of the ring are $Z_{s,z} = 38\ \Omega$ and $h_r = 7$ mm. The radial thickness of skin, capillary, and bone are changed by 50% and 20% with respect to the original model, where the result of the original model is shown with the black dotted line in Fig. 4(c). The results show that when the radial thickness of each layer is changed, the Mie-like resonance is stably excited, with a slight resonance frequency shift. The resonance frequency of each mode shifts from low to higher frequency when the thickness decreases. Therefore, if the thickness of each layer is provided in a calibration process, the monitoring can be performed with respect to the reference frequency measured with 0 wt % glucose-water solution. Figure 4(d) shows the magnitude of electric and magnetic fields at point d in Fig. 4(b). The field is localized following the circumference of the skin and capillary layers on the x-y plane. The field plot on the x-z plane also shows that both electric and magnetic fields are localized in the bilayer at the resonance frequency.

For the calculations so far, the glucose concentration inside the capillary has been kept at 0 wt %. To prove that the proposed ring structure is effective for noninvasively

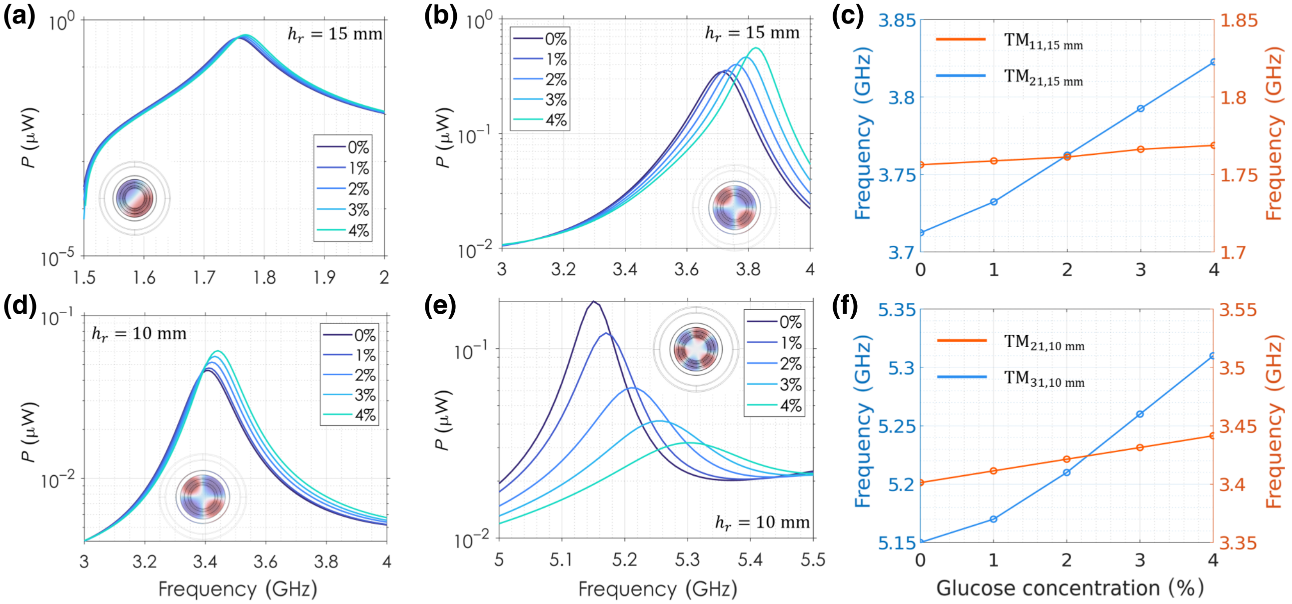

FIG. 5. (a) Radiated power $P_{\rm rad}$ around TM$_{11,15\rm mm}$ mode when $1/Y_{s,z} = -38$ Ω. (b) Radiated power $P_{\rm rad}$ around TM$_{21,15\rm mm}$ mode when $1/Y_{s,z} = -38$ Ω. (c) Comparison of frequency resolution of TM$_{11,15\rm mm}$ and TM$_{21,15\rm mm}$ with respect to glucose concentration. (d) Radiated power $P_{\rm rad}$ around TM$_{21,10\rm mm}$ mode when $1/Y_{s,z} = -38$ Ω. (e) Radiated power $P_{\rm rad}$ around TM$_{31,10\rm mm}$ mode when $1/Y_{s,z} = -40$ Ω. (f) Comparison of frequency resolution of TM$_{21,10\rm mm}$ and TM$_{31,10\rm mm}$ with respect to glucose concentration.

monitoring the glucose concentration, the refractive index of the capillary layer is then changed from 0 to 4 wt % in 1-wt % steps. The performance of glucose monitoring is quantified with the sensitivity S, which is defined as $S = \Delta f_s/\Delta$wt %, providing the frequency resolution of glucose detection [42,43]. The calculation is performed within the frequency bandwidth of each Mie-like resonance mode in Figs. 3 and 4, and the result is provided in Fig. 5. First, calculations are performed around TM$_{11}$ and TM$_{21}$ when $h_r = 15$ mm and $Z_{s,z} = 38$ Ω, and the results are provided in Figs. 5(a) and 5(b). For TM$_{11,15\text{ mm}}$, the resonance peak has almost no variation in the frequency axis, offering sensitivity $S = 3$ MHz/wt %. The derived sensitivity is 3 times smaller than the one in Ref. [37]. However, the TM$_{21,15\rm mm}$ mode provides a sensitivity of $S = 27.5$ MHz/wt %, almost 3 times and 9 times larger than in Ref. [37] and TM$_{11,15\rm mm}$, respectively. Figure 5(c) shows the comparison of the sensitivity between the two Mie-like resonance modes, TM$_{11,15\text{ mm}}$ and TM$_{21,15\rm mm}$. Here, the difference in sensitivity is visually emphasized, where the blue line denotes TM$_{21,15\rm mm}$ and the red line denotes TM$_{11,15\rm mm}$. Each mode provides linear step changes per glucose concentration, providing an efficient glucose monitoring scheme. Next, calculations around TM$_{21}$ and TM$_{31}$ are performed for $h_r =$ 10 mm. Here, the active load is $Z_{s,z} = 38$ Ω for TM$_{21}$ and $Z_{s,z} = 40$ Ω for TM$_{31}$, and results are provided in Figs. 5(d) and 5(e). The results show that TM$_{21,10\rm mm}$ provides a sensitivity $S = 10$ MHz/wt %, which is lower than TM$_{21,15\rm mm}$. For the TM$_{31,10\rm mm}$ mode, the resonance peak weakens with increasing glucose concentration. However, considering that the glucose concentration varies between 0 and 2 wt % for diabetes diagnosis, the TM$_{31,10\rm mm}$ can be also utilized. The TM$_{31,10\rm mm}$ mode offers a frequency step of 300–500 kHz per 0.01 wt % detection, which is the strongest sensitivity $S = 30-50$ MHz/wt %, in the proposed structure. The E_z field distributions are provided in each plot and show that the field is more localized inside the capillary and skin layer in the higher-order mode than the lower-order mode, which implies that the sensitivity increases when the modal order increases. The other property that can be observed by comparing Figs. 5(b) and 5(d) is that the sensitivity increases when the height of the ring increases. This property is attributed to the fact that the E_z field experiences a thicker capillary layer while resonating inside the finger. As a result, the sensitivity of TM$_{21,15\rm mm}$ is almost 3 times larger than TM$_{21,10\rm mm}$.

In conclusion, the proposed active loading of a dielectric ring offers an interesting platform to monitor the glucose concentration inside a finger by shifting Mie-like resonances. The sensitivity of our optimized active dielectric rings increases as the order of resonance increases, providing a sensitivity $S = 30-50$ MHz/wt %. Although blood is composed of various components and electrolytes, such as red blood cells, white blood cells, and NaCls, the calculation in our study assumes that the impact from other components is similar for all patients and stable in time, to show the reliability of the proposed technique. The exact measurement of glucose levels can be performed by calibrating a reference point, considering the finger dimensions, time since ingestion, temperature, and so on. The proposed method has a stable resonant response, and it provides a way to realize portable and practical glucose monitoring that can continuously detect glucose levels in real time and with enhanced sensitivity.

ACKNOWLEDGMENTS

This work was supported by the National Research Foundation, Republic of Korea Grant No. NRF-2021M3A 6B3037629, Global Frontier Projects and Grant No. NRF-2022R1G1A1010416, Basic Research Projects in Science and Technology, the Simons Foundation, and the National Science Foundation STC program.

[1] P. Boersma, L. I. Black, and B. W. Ward, Prevalence of multiple chronic conditions among US adults, 2018, Prev. Chronic Dis. **17**, E106 (2020).

[2] World Health Organization, Diabetes, 2023. (Diabetes (who.int))

[3] W. R. Rowley, C. Bezold, Y. Arikan, E. Byrne, and S. Krohe, Diabetes 2030: Insights from yesterday, today, and future trends, Popul. Health Manag. **20**, 1 (2017).

[4] Thaddäus Tönnies, Ralph Brinks, Scott Isom, Dana Dabelea, Jasmin Divers, Elizabeth J. Mayer-Davis, Jean M. Lawrence, Catherine Pihoker, Lawrence Dolan, Angela D. Liese, Sharon H. Saydah, Ralph B. D'Agostino, Annika Hoyer, and Giuseppina Imperatore, Projections of type 1 and type 2 diabetes burden in the U.S. population aged <20 years through 2060: The SEARCH for diabetes in youth study, Diabetes Care **46**, 313 (2023).

[5] K. Guk, G. Han, J. Lim, K. Jeong, T. Kang, E. K. Lim, and J. Jung, Evolution of wearable devices with real-time disease monitoring for personalized healthcare, Nanomaterials **9**, 813 (2019).

[6] Ali I. Siam, Mohammed Elaffendi, Atef Elsayed Abouelazm, Ghada El Banby, Nirmeen A. El-Bahnasawy, Fathi E. Abd El-Samie, and Ahmed A. Abd El-Latif, Portable and real-time IoT-based healthcare monitoring system for daily medical applications, IEEE Trans. Comput. Soc. Syst. **10**, 1629 (2022).

[7] Z. Deng, L. Guo, X. Chen, and W. Wu, Smart wearable systems for health monitoring, Sensors **23**, 2479 (2023).

[8] A. E. Macias, J. E. McElhaney, S. S. Chaves, J. Nealon, M. C. Nunes, S. I. Samson, B. T. Seet, T. Weinke, and H. Yu, The disease burden of influenza beyond respiratory illness, Vaccine **39**, A6 (2021).

[9] A. Ramachandran, Know the signs and symptoms of diabetes, Indian J. Med. Res. **140**, 579 (2014).

[10] K. Papatheodrou, M. Banach, E. Bekiari, M. Rizzo, and M. Edmonds, Complications of diabetes 2017, J. Diabetes Res. **2018**, 3086167 (2018).

[11] D. Tomic, J. E. Shaw, and D. J. Magliano, The burden and risks of emerging complications of diabetes mellitus, Nat. Rev. Endocrinol. **18**, 525 (2022).

[12] K. C. Park and H. J. Choi, Impaction of a continuous glucose monitoring sensor, Arch. Plast. Surg. **48**, 392 (2021).

[13] D. Rodbard, Continuous glucose monitoring: A review of successes, challenges, and opportunities, Diabetes Technol. Ther. **18**, 2 (2016).

[14] S. Seget, E. Rusak, M. Partyka, E. Samulska, A. Pyziak-Skupień, H. Kamińska, E. Skała-Zamorowska, and P. Jarosz-Chobot, Bacterial strains colonizing the sensor electrodes of a continuous glucose monitoring system in children with diabetes, Acta Diabetol. **58**, 191 (2021).

[15] W. V. Gonzales, A. T. Mobashsher, and A. Abbosh, The progress of glucose monitoring—A review of invasive to minimally and non-invasive techniques. devices and sensors, Sensors **19**, 800 (2019).

[16] H. Lee, Y. J. Hong, S. Baik, T. Hyeon, and D. H. Kim, Enzyme-based glucose sensor: From invasive to wearable device, Adv. Healthcare Mater. **7**, 1701150 (2018).

[17] Y. L. Yeh, Real-time measurement of glucose concentration and average refractive index using a laser interferometer, Opt. Lasers Eng. **46**, 666 (2008).

[18] T. Chang, H. Li, N. Zhang, X. Jiang, X. Yu, Q. Yang, Z. Jin, H. Meng, and L. Chang, Highly integrated watch for noninvasive continual glucose monitoring, Microsyst. Nanoeng. **8**, 25 (2022).

[19] A. J. Bandodkar, W. Jia, C. Yardimci, X. Wang, J. Ramirez, and J. Wang, Tattoo-based noninvasive glucose monitoring: A proof-of-concept study, Anal. Chem. **87**, 394 (2015).

[20] B. Todaro, F. Begarani, F. Sartori, and S. Luin, Is Raman the best strategy towards the development of non-invasive continuous glucose monitoring devices for diabetes management?, Front. Chem. **10**, 1 (2022).

[21] J. E. Park, N. Yonet-Tanyeri, E. V. Ende, A. I. Henry, B. E. P. White, M. Mrksich, and R. P. Van Duyne, Plasmonic microneedle arrays for in situ sensing with surface-enhanced Raman spectroscopy (SERS), Nano Lett. **19**, 6862 (2019).

[22] S. Pleus, S. Schauer, N. Jendrike, E. Zschornack, M. Link, K. D. Hepp, C. Haug, and G. Freckmann, Proof of concept for a new Raman-based prototype for noninvasive glucose monitoring, J. Diabetes Sci. Technol. **15**, 11 (2021).

[23] R. Pandey, S. K. Paidi, T. A. Valdez, C. Zhang, N. Spegazzini, R. R. Dasari, and I. Barman, Noninvasive monitoring of blood glucose with Raman spectroscopy, Acc. Chem. Res. **50**, 264 (2017).

[24] V. Tozzini and S. Luin, in *Fluorescent Proteins I. Springer Series on Fluorescence*, edited by Jung G. (Springer, Berlin, Heidelberg, 2011), Vol. 11.

[25] C. Song, W. H. Fan, L. Ding, X. Chen, Z. Y. Chen, and K. Wang, Terahertz and infrared characteristic absorption spectra of aqueous glucose and fructose solutions, Sci. Rep. **8**, 8964 (2018).

[26] J. Yadav, A. Rani, V. Singh, and B. M. Murari, in *2014 International Conference on Signal Processing and Integrated Networks (SPIN)* (Noida, India, 2014).

[27] J. L. Lai, S. Y. Huang, R. S. Lin, and S. C. Tsai, in *2016 International Conference on Applied System Innovation (ICASI)* (Okinawa, Japan, 2016).

[28] C. Bai, PhD (Doctor of Philosophy) thesis, University of Iowa, 2010. http://ir.uiowa.edu/etd/776.

[29] M. Wei, Y. Qiao, H. Zhao, J. Liang, T. Li, Y. Luo, S. Lu, X. Shi, W. Lu, and X. Sun, Electrochemical non-enzymatic glucose sensors: Recent progress and perspectives, Chem. Commun. **56**, 14553 (2020).

[30] D. Yang, S. Afroosheh, J. O. Lee, H. Cho, S. Kumar, R. H. Siddique, V. Narasimhan, Y. Z. Yoon, A. T. Zayak, and H. Choo, Glucose sensing using surface-enhanced Raman-mode constraining, Anal. Chem. **90**, 14269 (2018).

[31] M. Althobaiti, In silico investigation of SNR and dermis sensitivity for optimum dual-channel near-infrared glucose sensor designs for different skin colors, Biosensors(Basel) **12**, 805 (2022).

[32] A. E. Omer, G. Shaker, and S. Safavi-Naeini, Non-invasive glucose monitoring at mm-wave frequencies, J. Comput. Vis. Imaging Syst. **4**, 3 (2018).

[33] M. Baghelani, Z. Abbasi, M. Daneshmand, and P. E. Light, Non-invasive continuous-time glucose monitoring system using a chipless printable sensor based on split ring microwave resonators, Sci. Rep. **10**, 12980 (2020).

[34] H. Canogarcia, P. Kosmas, I. Sotiriou, I. Papadopouloskelidis, C. Parini, I. Ioannis Gouzouasis, G. Palikaras, and E. Kallos, Detection of glucose variability in saline solutions from transmission and reflection measurements using V-band waveguides, Meas. Sci. Technol. **26**, 125701 (2015).

[35] S. Saha, H. Cano-Garcia, I. Sotiriou, O. Lipscombe, I. Gouzouasis, M. Koutsoupidou, G. Palikaras, R. Mackenzie, T. Reeve, P. Kosmas, and E. Kallos, A glucose sensing system based on transmission measurements at millimeter waves using micro strip patch antennas, Sci. Rep. **7**, 6855 (2017).

[36] Li Ge, Y. D. Chong, and A. D. Stone, Conservation relations and anisotropic transmission resonances in one-dimensional PT-symmetric photonic heterostructures, Phys. Rev. A **85**, 023802 (2012).

[37] Y. J. Zhang, H. Kwon, M. A. Miri, E. Kallos, H. Cano-Garcia, M. S. Tong, and A. Alù, Noninvasive glucose sensor based on parity-time symmetry, Phys. Rev. Appl. **11**, 044049 (2019).

[38] C. G. Varas and T. J. U. Thompson, Metric dimensions of the proximal phalanges of the human hand and their relationship to side, position, and asymmetry, HOMO **62**, 126 (2011).

[39] S. Gabriel, R. W. Lau, and C. Gabriel, The dielectric properties of biological tissues: III. Parametric models for the dielectric spectrum of tissues, Phys. Med. Biol. **41**, 2271 (1996).

[40] Venkataraman and B. Freer, in *2011 IEEE International Symposium on Antennas and Propagation (APSURSI), Spokane, WA, USA* (2011).

[41] M. Hofmann, G. Fischer, R. Weigel, and D. Kissinger, Microwave-based noninvasive concentration measurements for biomedical applications, IEEE Trans. Microwave Theory Tech. **61**, 2195 (2013).

[42] B. F. Wan, B. X. Li, and H. F. Zhang, Theoretical study of dual-function sensor for analysis of blood composition and glucose concentration based on nonreciprocal analog of the electromagnetically induced absorption, IEEE Trans. Instrum. Meas. **72**, 7007610 (2023).

[43] P. S. Maji, M. K. Shukla, and R. Das, Blood component detection based on miniaturized self-referenced hybrid Tamm-plasmon-polariton sensor, Sens. Actuators, B **255**, 729 (2018).